Review Article

Multiferroic and Optical Properties of La$_{0.05}$Li$_{0.85}$NbO$_3$ and LiNbO$_3$ Nanocrystals

Carlos A. Díaz-Moreno [ORCID],[1] **Jorge A. López,**[2] **Yu Ding,**[2] **A. Hurtado Macias,**[3] **Chunqiang Li,**[2] **and Ryan B. Wicker**[1]

[1]*W. M. Keck Center for 3D Innovation, Collage of Engineering E-108, University of Texas at El Paso, 500 W. University Ave., El Paso, TX 79968, USA*
[2]*Department of Physics, University of Texas at El Paso, El Paso, TX, USA*
[3]*Centro de Investigación en Materiales Avanzados S.C., Miguel de Cervantes No. 120 Complejo Industrial Chihuahua, 31109 Chihuahua, Chih., Mexico*

Correspondence should be addressed to Carlos A. Díaz-Moreno; cdiazmoreno@utep.edu

The chemistry and physics of surfaces is an increasingly important subject. The study of surfaces is the key of many important nanotechnological applications due to the understanding of phase transitions, electronic structure, and chemical bonding. In later years, exotic phenomena that jointly involve the magnetic and electrical conductivity properties have been discovered in oxides that contain magnetic ions. Moreover, the uses of magnetic oxides in electronic technology have become so important due to the miniaturization of devices and magnetic materials with dielectric properties or vice versa being required for inductors, information storage, thin films for high-density computer memories, microwave antireflection coatings, and permanent magnets for automobile ignitions among others. On the contrary, nanotechnology developments over 10 years or so have provided intensive studies in trying to combine properties such as ferroelectric, ferromagnetic, and optics in one single-phase nanoparticles or in composite thin films; this last effort has been recently known as multiferroic. Because of this, the resurgence of nanomaterials with multiferroic and optical properties is presented in this work of one single phase in lanthanum lithium niobate (La$_{0.05}$Li$_{0.85}$NbO$_3$) and lithium niobate (LiNbO$_3$) with ferromagnetic, ferroelectric, relaxor ferroelectricity, second harmonic generation, high-temperature ferromagnetic, and magnetoelectric properties.

1. Introduction

Recent studies have discovered exotic phenomena that involve jointly magnetic and electrical properties of oxides with magnetic ions [1]. These new properties of the magnetic oxides have been rapidly adapted in the electronic industry, which requires magnetic materials with dielectric properties for inductors, memory storage, microwaves antireflection coatings and so on. [2, 3]. This is creating a new area of the nanotechnology industry that combines ferroelectric, ferromagnetic, and optical properties in one single-phase nanoparticles or in composite thin films, known as multiferroic [4–6]. Some examples of

ferromagnetic materials are metals such as cobalt, iron, nickel, various alloys, semimetallic compounds with rare earths, transition elements, and numerous ceramics [7].

1.1. Ferroelectricity, Ferromagnetism, and Ferroics. The magnetoelectric effects found in magnetic oxides have recently found numerous applications in biology, medicine, and biotechnology [8]. Ferroelectricity is a property of noncentrosymmetric dielectric materials, which have at least two thermodynamically stable orientation states that can be exchanged under the influence of an external electric field (**E**) and whose only difference is the direction of the polarization vector (**P**). The observable physical effect is that the material

presents a remnant polarization ($\mathbf{P_r}$) after eliminating the electric field ($\mathbf{E} = 0$) [9, 10]. The explanation is the appearance of permanent dipoles. Ferroelectric oxides with ABO_3 perovskite crystal structures with high dielectric constant (κ) have been attracting lots of attentions due to its combination of properties, such as pyroelectric, piezoelectric, ferroelectric-magnetic, and electro-optical, in single-phase nanoparticles and composites [6, 10, 11].

On the contrary, ferromagnetism is a physical phenomenon in which a magnetic ordering of all the magnetic moments ($\mathbf{m}$) of a material with the same direction takes place. A ferromagnetic material is one that can present ferromagnetism ($\mathbf{m_s}$) [12, 13]. In general, ferromagnets are divided into magnetic domains and separated by surfaces known as Bloch walls. In each of the domains, the magnetic moments are aligned in some direction according to the axis of easy magnetization.

The original definition of a multiferroic material is that it has two of three primary ferroic properties: ferroelectricity (FE), ferromagnetism (FM), and ferroelasticity [14]. The coupling between the ferroelectric and ferromagnetic property distributions can be through the coupling of the spontaneous polarization ($\mathbf{P_s}$) of ferroelectric materials and the spontaneous ferromagnetic magnetization ($\mathbf{m_s}$), but this magnetoelectric coupling does not happen automatically [15]. The magnetoelectric coupling can arise directly through the induction of voltages or indirectly when induced by stress [16].

1.2. Characterization Tools.

In the last decade, there has been an increasing effort to characterize multiferroic materials by using different techniques [17, 18], namely, with diverse spectroscopic and nonlinear optical and surface characterization techniques. The recent advances in small-scaled electronics, combined with computational equipment had allowed microscopy analysis in STEM Cs-corrected to study the surface (shell) and core (bulk) of core-shell nanoparticles [19]. Consequently, new information regarding structural aspects of nanoparticles is possible to obtain using the following surface of characterization techniques.

1.2.1. Electron Energy Loss Spectroscopy.

One characterization technique used for this type of multiferroic materials is electron energy loss spectroscopy (ELLS). The interaction of electrons with materials provides structural and chemical information [20]; EELS studies the vibration of atoms and molecules near the surface of a sample [21]. Electrons with energies between 0.1 and 10 keV lose energy by interacting with oscillating dipoles produced by the vibration modes of the sample molecules, and thus provide information about the orientation (normal or parallel) of the molecule's polarization. EELS is a suitable tool to detect dispersed chemical species in the volume and surface of nanoparticles.

1.2.2. Raman Spectroscopy.

Raman spectroscopy provides useful information about vibration-rotational spectroscopy of crystalline solid samples [22]; it is based on molecular deformation in electric field ($\mathbf{E}$) determined by polarizability (α) of laser light. The properties of the materials can be influenced by their particle size, stoichiometry, chemical homogeneity, mechanical stresses, and phase transition, so that Raman spectroscopy is suitable to correlate structural modifications due to dopants or new synthesis of solid solutions providing a fingerprint of materials.

1.2.3. X-Ray Photoelectron Spectroscopy.

XPS is based on the photoelectric effect, and it provides information about the composition of surface elements with valuable quantitative and chemical state information from top ∼5 nm of the surface of a material [21]. It uses a beam of X-rays which interact with core electrons from the surface atoms freeing them with a kinetic energy indicative of their former binding energy, which is used to identify the atom from which the electrons were released, as well as the binding state of such atom.

1.2.4. Second Harmonic Microscopy.

The second harmonic generation (SHG) microscope is used to study second order nonlinear optical processes which may exist in materials with nonlinear properties. The effect of frequency doubling, in which initial photons interact with the nonlinear material, produces photons with twice the energy and frequency and half the wavelength of the initial photons; this effect is useful for imaging of materials without inversion symmetry. The optical response of such a medium to an applied electromagnetic field can be expressed in terms of its polarization density $\mathbf{P}(t)$, which, in linear dielectric media, can be written as a linear function with frequency doubling generated due to their chemical composition, polarization, and susceptibility [23].

1.2.5. Cs-Corrected Scanning Transmission Electron Microscope.

Aberration-corrected electron microscopy allows subangstrom resolution in high-resolution transmission electron microscopy. Aberration-corrected high-resolution scanning transmission electron microscopy can provide detailed interfacial structure information, such as maps of lattice displacements, misfit dislocations, strain fields, termination planes, cation disorder, and substrate terraces. In particular, its use combined with magnetic fields and electromagnetic lenses leads to atomic resolution images that are essential for measuring crystalline structures and composition intimately related to the properties of smart materials. This technique of characterization of high spatial resolution images has become an important tool for the evaluation and development of new nanotechnology materials and devices [24].
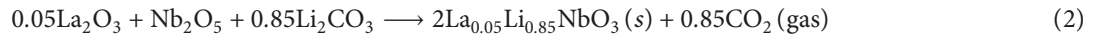
1.3. Materials.

Perovskite structure types are an ideal candidate material for nonlinear optical applications; these include $PbTiO_3$, $Pb(Zr,Ti)O_3$, $Pb(Fe_{1/2}Nb_{1/2})O_3$, $Pb(Fe_{0.5}Ta_{0.5})O_3$, $Pb(Fe_{1-x}Nb_x)O_3$ and $Ni_{0.35}Zn_{0.65}Fe_2O_4$, $Pb(Mg_{1/3}Nb_{2/3})O_3$ (PMN), $Pb(Sc_{1/2}Ta_{1/2})O_3$ (PST), and $Pb_{1-x}La_x(Zr_{1-y}Ti_y)_{1-x/4}$ (PLZT) [3, 10, 14, 25]. However, in the last decade, intensive efforts have tried to substitute lead in piezoelectric PZT by a less harmful lead-free piezoelectric-ferroelectric/ferromagnetic materials [26–28]. Furthermore, the development of lead-free ABO_3 nanomaterials has created a new variety of compounds such as $LiNbO_3$, which has attracted

much attention in both scientific and application fields [11]. Due to its availability, widespread use, and versatility, lithium niobate, $LiNbO_3$ (LN), is one of the most promising ferroelectric materials, characterized by high Curie temperatures ($T_c = 1210°C$), band gap ($E_g = 3.7$ eV), and piezoelectric and electro-optical coefficients. LN has a wide range of applications; in particular, it has been used in artificial photosynthesis to reduce effects of global warming [29], in storage of hydrogen produced by splitting water under UV light radiation [30], and others.

1.4. Summary. In this article, we present results of our research of ferroelectric, ferromagnetic, and optical properties of smart ceramic nanomaterials, such as lanthanum lithium niobate and lithium niobate synthesized by the mechanochemical method. The purpose of our studies is to characterize this material through Cs-STEM, EELS, Raman, XPS, and SHG to start understanding how the spatial position of atoms in the crystalline structure of multiferroic materials correlates with its properties.

2. Experimental Details

2.1. Stoichiometric Preparation of $LiNbO_3$ and $La_{0.05}Li_{0.85}NbO_3$ Nanoparticles. In the past, we have synthesized lanthanum lithium niobate ($La_{0.05}Li_{0.85}NbO_3$) and lithium niobate ($LiNbO_3$) nanocrystals with ferromagnetic, magnetoelectric, relaxor ferroelectricity, and optic properties by using mechanochemical alloying followed by a reduction heat treatment (RHT) process [31, 32]. In the present study, we synthesize stoichiometric lanthanum lithium niobate ($La_{0.05}Li_{0.85}NbO_3$) and lithium niobate ($LiNbO_3$) by using lithium carbonate (Li_2CO_3), niobium oxide (Nb_2O_5), and lanthanum oxide (La_2O_3) as precursors. These precursors are of high-purity (99.99%) and are commercially available from Alfa Aesar; they are mixed by mechanical milling during 300 minutes in a SPEX Series 8000M with mixture/balls relation of 0.1, followed by a heat treatment of calcinations at 650°C in a Thermolite 2136 in air atmosphere, producing nanocrystals of the ferroelectrical phase of $LiNbO_3$ and $La_{0.05}Li_{0.85}NbO_3$. The solid-state reactions involved are as follows:

$$Nb_2O_5\,(s) + Li_2CO_3\,(s) \longrightarrow 2LiNbO_3\,(s) + CO_2\,(gas) \tag{1}$$

$$0.05La_2O_3 + Nb_2O_5 + 0.85Li_2CO_3 \longrightarrow 2La_{0.05}Li_{0.85}NbO_3\,(s) + 0.85CO_2\,(gas) \tag{2}$$

Furthermore, temperature-programmed reduction was conducted to generate oxygen vacancies related with ferromagnetic, magnetoelectric, relaxor ferroelectricity, and optic properties in $La_{0.05}Li_{0.85}NbO_3$ and $LiNbO_3$ on single-phase nanocrystals. Ferroelectrical samples were then annealed by reduction heat treatment (RHT) in an Ar-5%H_2 atmosphere for 20 minutes at 900°C. A grey coloration was observed instead of the white powder before the RHT process.

2.2. EELS and Cs-Corrected Scanning Transmission Electron Microscope. The electron energy loss spectroscopy and high-resolution images were obtained using a JEOL ARM (200F) microscope at the Research Center of Advanced Materials (RCAM) of Chihuahua-Mexico, operating at 200 kV, equipped with a Cs corrector (CEOS GmbH) and a FEG-STEM/TEM unit. The high-angle annular dark-field (HAADF) probe size was set to 0.095 nm, and a current of 23.2 pA was used for bright-field imaging. Condenser lens aperture sizes were set to 40 μm. A camera length (CL) of 8 cm/6 cm and collection angle of 68–280 mrad/90–270 mrad was chosen in order to eliminate contributions from unscattered beams. The ELLS spectrometer was carried out on JEOL-2200 FS HR-FE-TEM equipment, equipped with an energy filter column (filter-Ω) and with a spatial resolution of 0.16 nm, and sample preparation was as previously reported [32, 33].

2.3. Surface Characterization: Raman and X-Ray Photoelectron Spectroscopy. Raman spectroscopy was made using a Micro LabRAM HR model (Lexc = 632.8 nm) at the RCAM, within a range from 100 to 1000 cm^{-1}, with a 14 mW laser excitation power by using a 100x objective and an aperture of ~1 micron. The X-ray photoelectron spectroscopy (XPS) analyses were carried out at the University of Texas at El Paso with a PHI 5600 spectrometer with a hemispherical energy analyzer, using magnesium (MgK_α) source of 1253.6 eV at 100 Watts. The pressure in the analysis chamber during XPS analysis was in the low range of 10^{-9} Torr. All spectra were recorded at 54° take-off angle, the analyzed area being currently about 1 mm^2. All spectra were recorded with 1.0 eV step, 10 cycles, and 20 sweeps and corrected using carbon signal (C1s) at 284.5 eV. XPS spectra were analyzed using Casa-XPS software version 2.3.12. The Shirley method was used for extracting the background necessary for curve fitting.

2.4. Ferroelectric, Magnetic, Dielectric, and Magneto-capacitance Measurements. Ferroelectric measurements were performed using an Agilent E4980A 20 Hz–2 MHz precision LCR meter at the Center of Nanoscience and Nanotechnology (CNN) of the National Autonomous University of Mexico. At 300 K, the particles were bounded with PVA and pressed at 105 kg/cm^2; diameter (ϕ) was of 11.7 mm and height (h) of 1 mm. Magnetization measurements were performed at the RCAM using a Physical Property Measurements (PPMS) equipment model 9 *T*

(Quantum Design) with a vibrating sample magnetometer. On the contrary, dielectric measurements were performed at the CNN using a Hewlett Packard 4284A 20 Hz–1 MHz precision LCR Meter with Control Temperature (Eurotherm). The experiment conditions were using a frequency from 100 Hz to 1 MHz, temperature rate of 5°C/min, and 1 volt of oscillation. The magnetocapacitance effect was measured using Agilent E4980A equipment from 20 Hz to 2 MHz precision LCR meter coupled to VersaLab 3 Tesla (Quantum Design) with a vibrating sample magnetometer; sample preparation as previous reported [34].

2.5. Second Harmonic Generation Microscope.
The scanning second harmonic generation microscopy was performed at the University of Texas at El Paso using a femtosecond Ti: sapphire laser source (Spectra-Physics, Mai Tai SP). Its pulse duration is about 100 fs with a repetition of 80 MHz. The wavelength of the laser is tunable from 690 nm to 1040 nm, with the maximum power up to 2.5 W. The fundamental laser beam is tightly focused by a 60x NA 1.0 water-immersion objective lens (Olympus LUMPlanFLN). The generated SHG signal is collected by the same objective lens in an epi-detection geometry. The signal is separated from noise by a dichroic mirror and a 20 nm narrow band pass filter centered at 450 nm. The schematic illustration of the experimental setup is shown in Figure 1.

3. Results and Discussion

3.1. EELS and Cs-Corrected Scanning Transmission Electron Microscope.
Using Cs-corrected high-resolution transmission electron microscope in scanning mode, it was possible to determine structural aspects for RHT and non-RHT at the surface of $LiNbO_3$ sample. Figures 2(a) and 2(b) are representative Cs-corrected STEM images of the crystal lattice with no-RHT and with RHT at 2 nm scale of $LiNbO_3$, respectively.

It is observed that the crystal lattice remains constant with no-RHT, unlike when compared to crystal lattice with RHT, that clearly observes voids in its crystalline structure. Figures 2(c) and 2(d) show that the interatomic profile of the crystalline lattice with no-RHT is 0.37 nm and with RHT is 0.34 nm, respectively. It can be seen from the interatomic profile results that crystal lattice has a decrease in length and intensity due to the RHT at surface of $LiNbO_3$ nanocrystals.

Furthermore, Figures 3(a) and 3(b) show the selected area diffraction (SAD) of samples before and after the RHT process.

The crystalline SAD diffraction lattice of $LiNbO_3$ with no-RHT remains constant with a perfect hexagonal lattice, with the principal diffraction directions at [110], [116], and [312], as related to the stoichiometric ferroelectric $LiNbO_3$ phase. The $LiNbO_3$ corresponds to the trigonal/rhombohedral crystal structure with lattice parameters at $a = b = 5.142$ Å, and $c = 13.843$ Å and angles $\alpha = \beta = 90°$ and $\gamma = 120°$ associated to R3cH space group [11, 32]. The SAD patterns with RHT atoms do not have a uniform arrangement due to the formation of surface defects of $LiNbO_3$. The creations of lattice defects are
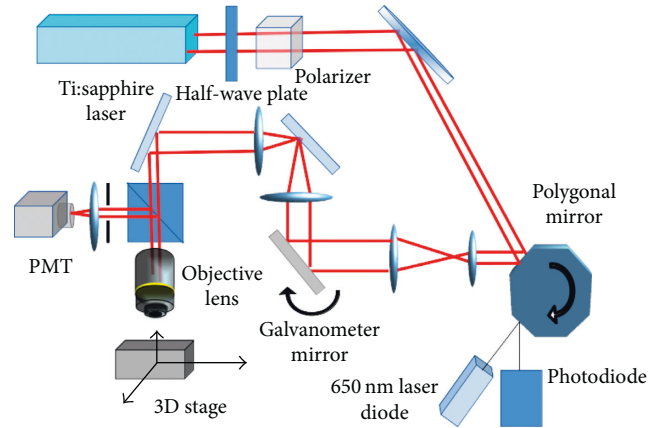

FIGURE 1: Experimental setup for second harmonic generation imaging.

related to oxygen vacancies, diffusion of Li atoms, and disordered atoms at the surface of nanoparticles as previously reported for $LiNbO_3$ and $La_{0.05}Li_{0.85}NbO_3$, respectively [32, 35]. In addition, ferromagnetism appears after oxygen depletion, which has been confirmed for other materials with ABO_3 perovskite structure [35, 36]. It is well known that oxygen vacancies are also responsible for the relaxor ferroelectricity behavior in ABO_3 perovskite systems [25, 31, 37, 38].

On the contrary, the bulk and surface in multiferroic $LiNbO_3$ can differ in structure, composition, and properties as found by Sanna and Schmidt [39]. The multiferroic $LiNbO_3$ core-shell nanoparticles were studied by EELS spectroscopy. Figure 3(c) shows the energy loss spectrum of the core (bulk) and the surface (shell) as reported before [32, 33]. The core plot has a dominant peak that corresponds to a plasmon around 14.55 eV. In addition, they are less intense peaks before the plasmon around the 4.06 eV and 8.7 eV; the energy loss at 4.06 eV corresponds to the carbon atoms, and that at 8.7 eV corresponds to the electronic orbital of the 2p-orbital associated with oxygen. The 14.55 eV plasmon is attributed to the octahedron bond vibrations NbO_6 at 23.2 eV to lithium, and at 27 eV to the plasmon attributed to the vibrations of octahedral LiO_6, similarly to what was determined by Mukhtarov et al. [40]. The shell spectrum shows most outstanding peaks at 6.13 eV, 11.17 eV, 20.34 eV, and 30.9 eV. The well-defined maximum around 11.17 eV is due to the plasmon next to the octahedrons of oxygen. The peak at 6.13 eV corresponds to interband electronic transitions related to the paraelectric phase of the ferromagnetic surface due to the superficial vacancies of oxygen in nanocrystals of multiferroic $LiNbO_3$. The band at 20.34 eV is attributed to the vibrations of the octahedron LiO_6, and at the 39.9 eV is a plastic excitation, related to the vibration of the lattice, which corresponds to niobiums within oxygen octahedrons. The energies 2.8 eV, 3.3 eV, and 3.8 eV are related to the ferromagnetic origin of the ferroelectric $LiNbO_3$.

The peaks in the imaginary part of the dielectric function originate due to transitions between bands in the ferroelectric region and the ferromagnetic surface, which can be the mechanism that occurs in multiferroic $LiNbO_3$ nanocrystal single phase. This loss of energy is related to the electrons
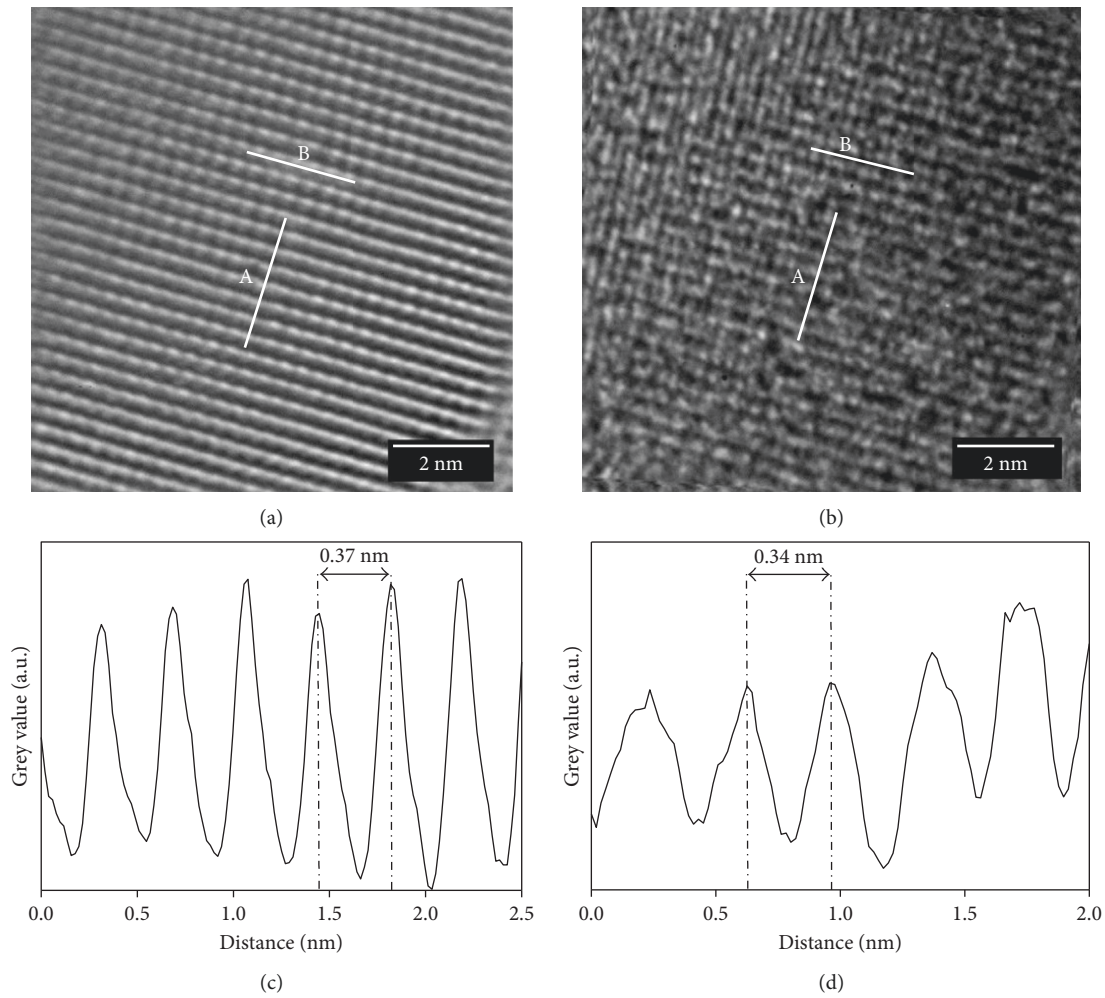
(a)

(b)

(c)

(d)

FIGURE 2: Cs-corrected scanning electron microscope: (a) LiNbO$_3$ lattice with no RHT; (b) LiNbO$_3$ lattice after the RHT; (c) interatomic distance with no RHT; (d) interatomic distance with RHT.

due to the oscillating dipoles present in the ferromagnetic surface. These dipoles are due to the vibration modes of the molecular absorbers present. These results suggest a ferroelectric/paraelectric-magnetic interface with the ferromagnetic at surface, as reported by some other works for ZnO and BaTiO$_3$ [41, 42]. The existence of well-defined collective excitations (plasmon) can determine the electronic density in the valence and conduction bands that intervene in the collective oscillations between the ferroelectric region and the ferromagnetic surface in the multiferroic LiNbO$_3$ nanocrystals. The found values were a core-shell electronic density of 1.79×10^{29} and 1.33×10^{29} in electron/m^3, respectively. The electron density for the valence and the electron conduction bands is much higher for the ferroelectric region than that for the ferromagnetic surface. In the case of having a polar surface of the LiNbO$_3$, the positive and negative surfaces have a different stoichiometric structure. The dielectric loss results at the surface of multiferroic LiNbO$_3$ nanocrystals is due to appearance of Nb^{+4} related to paraelectric phase due to the interband electronic transitions caused by the presence of oxygen vacancies at the surface in complete agreement with the reported before [33, 35, 43]. In addition, this can also be understood by the intrinsic covalent character present in the LiNbO$_3$ structure in the form of Li-O-(Nb=O)$_2$ [11, 40]. This EELS results were in complete agreement with similar EDS studies performed for oxygen and niobium profiles as previously reported [35].

3.2. Surface Characterization: Raman Spectroscopy and XPS. The multiferroic La$_{0.05}$Li$_{0.85}$NbO$_3$ and LiNbO$_3$ single-phase core-shell nanocrystals were studied with Raman spectroscopy and XPS due to their different chemical compositions at the surface due to lattice defects, oxygen vacancies, Li atoms diffusion, and La atoms order-disordered. Figures 4(a) and 4(b) show the Raman spectrum survey of stoichiometric LiNbO$_3$ and La$_{0.05}$Li$_{0.85}$NbO$_3$ at room temperature from 100 cm^{-1} to 1000 cm^{-1}, respectively. The vibrational modes found are at 153, 185, 239, 260, 276, 303, 322, 334, 370, 433, 451, 581, 625, 694, 877 cm^{-1} and 153, 186, 238, 256, 276, 302, 323, 333, 369, 433, 451, 581, 624, 680, and 876 cm^{-1}, respectively [31, 34, 44, 45]. The vibration modes at 260 (256), 276, and 322 (323) cm^{-1} are related to LiO$_6$ octahedron, the diffusion of Li-O bonds, the O-Nb-O bond, and the

(a)

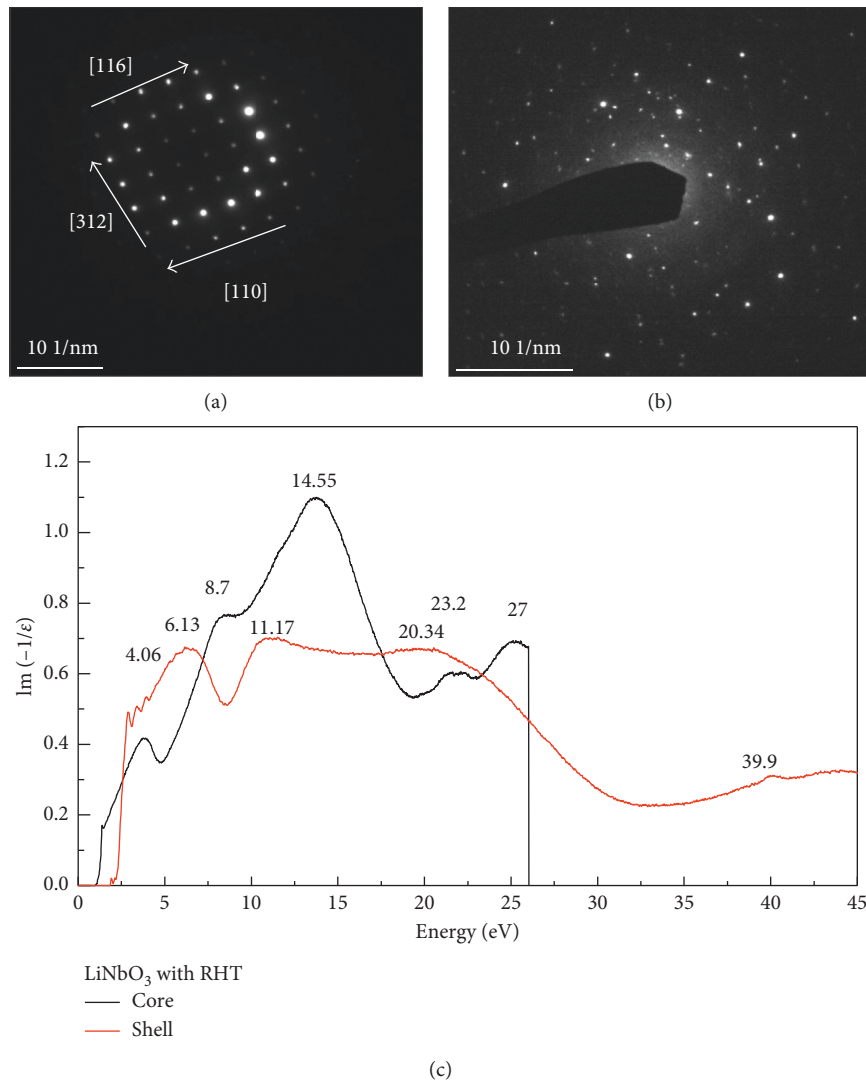(b)

LiNbO₃ with RHT
— Core
— Shell

(c)

FIGURE 3: (a) Selected area diffraction with no RHT; (b) selected area diffraction after the RHT; (c) EELS spectrum. Black plot related to the core, and red plot related to the shell.

diffusion of Li-O atoms at surface during RHT. The vibration modes of the octahedral NbO_6 site are at 581, 625 (624), and 694 (680) cm^{-1}, related to ferroelectric and ferromagnetic phase. The vibrational modes at 276, 322 (323), and 625 (624) cm^{-1} correspond to the vibration modes A_1 [TO_2], A_1 [TO_3], and A_1 [TO_4] associated with loss of symmetry of oxygen site that is produced during the RHT.

On the contrary, Figures 4(c) and 4(d) are showing the binding energies found on the XPS results, which are related to the electronic orbital structure of lithium (Li^{+1}), lanthanum (La^{+3}), niobium (Nb^{+5}), and oxygen (O^{-2}) in multiferroic $LiNbO_3$ and $La_{0.05}Li_{0.85}NbO_3$, respectively. In Figure 4(c), the Nb 3d-orbital and O 1s-orbital are associated to the multiferroic properties. The niobium Nb 3d-orbital binding energies are at 209.9 eV, 207.8 eV and 205.7 eV, ascribed to Nb^{5+}, Nb^{4+} and Nb^{3+} ions associated to concentration of oxygen voids occurred mainly during the RHT. The oxygen O 1s-orbital binding energy results are at 529.4 eV, 532 eV, and 534.1 eV. The signal at 529.4 eV is associated with the natural

network of $LiNbO_3$, which is reduced due to the reordering in the network shown in 532 eV and 534.1 eV signal is associated with oxygen vacancies (O^*), as previously reported [34, 46]. In Figure 4(d), the electronic structure of stoichiometric $La_{0.05}Li_{0.85}NbO_3$ is related to O 2s-orbital (20.7 eV), La 5s-orbital (33.9 eV), lithium (Li) 1s-orbital (59.1 eV), La $4d_{5/2}$-orbital (101.1 eV), La $4d_{3/2}$-orbital (103.3 eV), Nb-$3d_{5/2}$-orbital (206.1 eV), Nb-$3d_{3/2}$-orbital (208.2 eV), C 1s-orbital (283.7 eV), Nb-$3p_{3/2}$-orbital (364.1 eV), Nb-$3p_{1/2}$-orbital (379.7 eV), and O 1s-orbtial (529.1 eV) related to the natural network of La-Li-Nb-O₃ previously reported [31, 47, 48]. In addition, from XPS results, the degree of ionicity of Nb $d_{5/2}$-orbital was found a chemical shift of 1.3 eV, and for O 1s-orbital were found two chemical shifts at 4.7 eV and 2.2 eV, which are attributed to the appearance of Nb^{4+} and oxygen vacancies due to the RHT in $La_{0.05}Li_{0.85}NbO_3$ when compared to $LiNbO_3$, respectively. The XPS results found in $LiNbO_3$ nanocrystals are in complete agreement with the results found in Cs-STEM-SAD and ELLS.
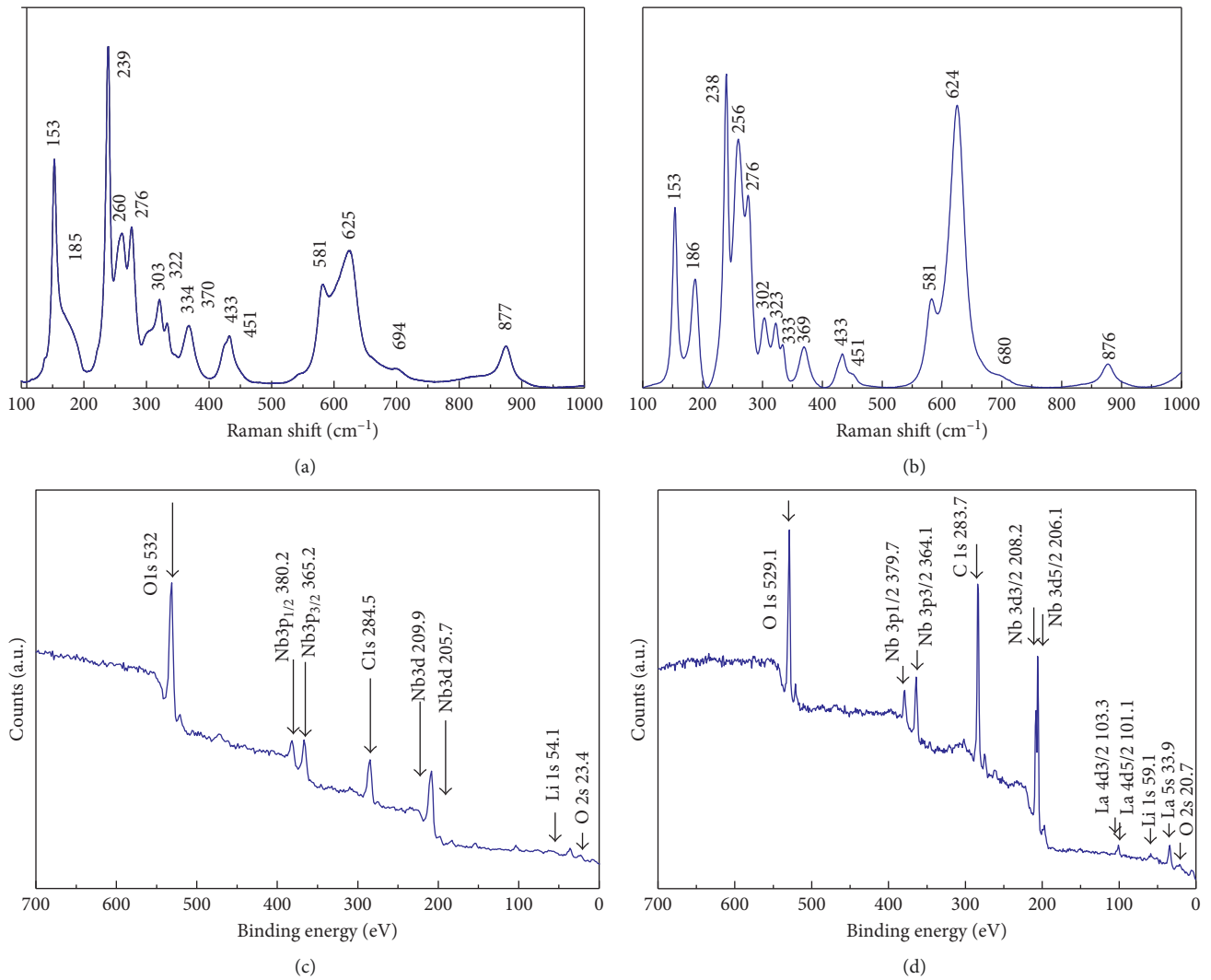
(a)

(b)

(c)

(d)

FIGURE 4: Raman spectrum of multiferroic: (a) $LiNbO_3$ and (b) $La_{0.05}Li_{0.85}NbO_3$. XPS spectrum of multiferroic: (c) $LiNbO_3$ and (d) $La_{0.05}Li_{0.85}NbO_3$.

3.3. Multiferroic Properties in $LiNbO_3$ and $La_{0.05}Li_{0.85}NbO_3$ Nanocrystals: Ferroelectric, Ferromagnetic, Magnetocapacitance, and Relaxor Ferroelectricity Measurements.

$LiNbO_3$ and $La_{0.05}Li_{0.85}NbO_3$ nanocrystals single phase can be endowed with multiferroic properties (such as ferroelectric, ferromagnetic, magnetocapacitance, and relaxor ferroelectricity) by the creation of oxygen vacancies at the surface of nanocrystals.

3.3.1. Ferroelectric.

The ferroelectric property of $LiNbO_3$ and $La_{0.05}Li_{0.85}NbO_3$ was characterized through polarization-electric field hysteresis loop. Figures 5(a) and 5(b) show the polarization-electric field (P-E) loop of $LiNbO_3$ and $La_{0.05}Li_{0.85}NbO_3$ at room temperature, respectively. The ferroelectric properties of $LiNbO_3$ values found at saturation polarization, remnant polarization, and coercive field are ($P_s = 0.0701\,\mu C/cm^2$), ($P_r = 0.0382\,\mu C/cm^2$), and ($E_c = 3.8\,kV/cm$), respectively. The ferroelectric properties of $La_{0.05}Li_{0.85}NbO_3$ were found at ($P_s = 0.235\,\mu C/cm^2$), ($P_r = 0.141\,\mu C/cm^2$), and ($E_c = 1.35\,kV/cm$), respectively

[31, 32]. This P-E is "nonideal" due to the relatively high leakage caused by the existence of oxygen vacancies at the surface. In addition, the presence of lanthanum in $La_{0.05}Li_{0.85}NbO_3$ increases the ferroelectric signals when it is compared to pure lithium niobate ($LiNbO_3$).

3.3.2. Ferromagnetic.

The ferromagnetic properties were also analyzed. Figures 6(a) and 6(b) show the ferromagnetic properties in $LiNbO_3$ and $La_{0.05}Li_{0.85}NbO_3$ nanocrystals; these clearly show an anhysteretic ferromagnetic curve at room temperature with a saturation magnetization of 7.53×10^{-4} emu/g and 2.5×10^{-3} emu/g, respectively. In addition, Figure 6(a) shows the lithium niobate magnetization curves at 300, 200, 150, 100, 50, and 4 K and shows the sample without RHT (not magnetic signal) with a magnetic behavior characteristic of dilute magnetic oxides and other undoped oxides, originating at the superficial region known as high-temperature ferromagnetic behavior. Anhysteretic magnetic curves show no temperature dependence in a wide range of temperature (4–300 K). Such
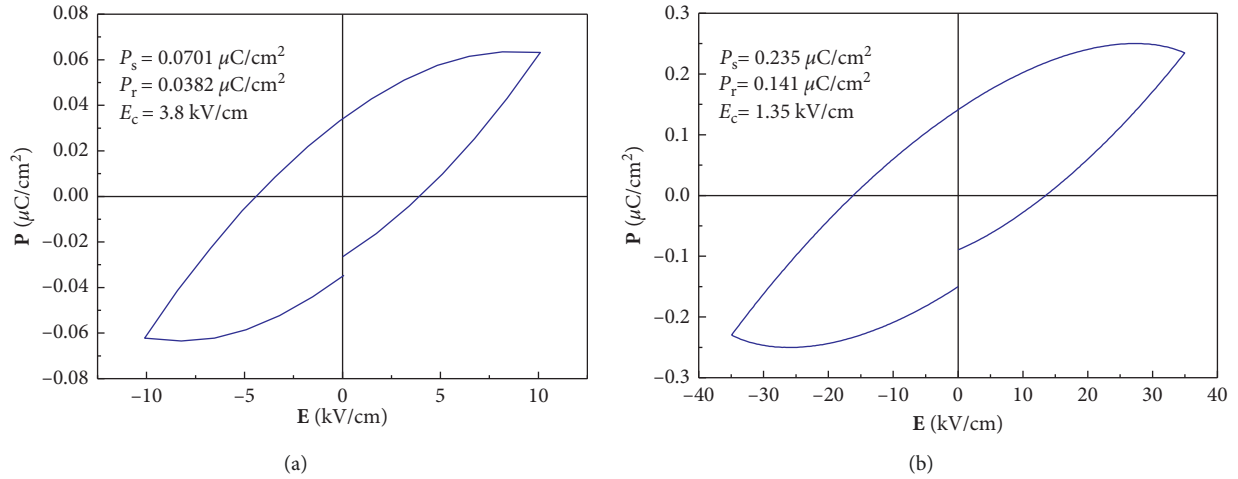
(a)

(b)

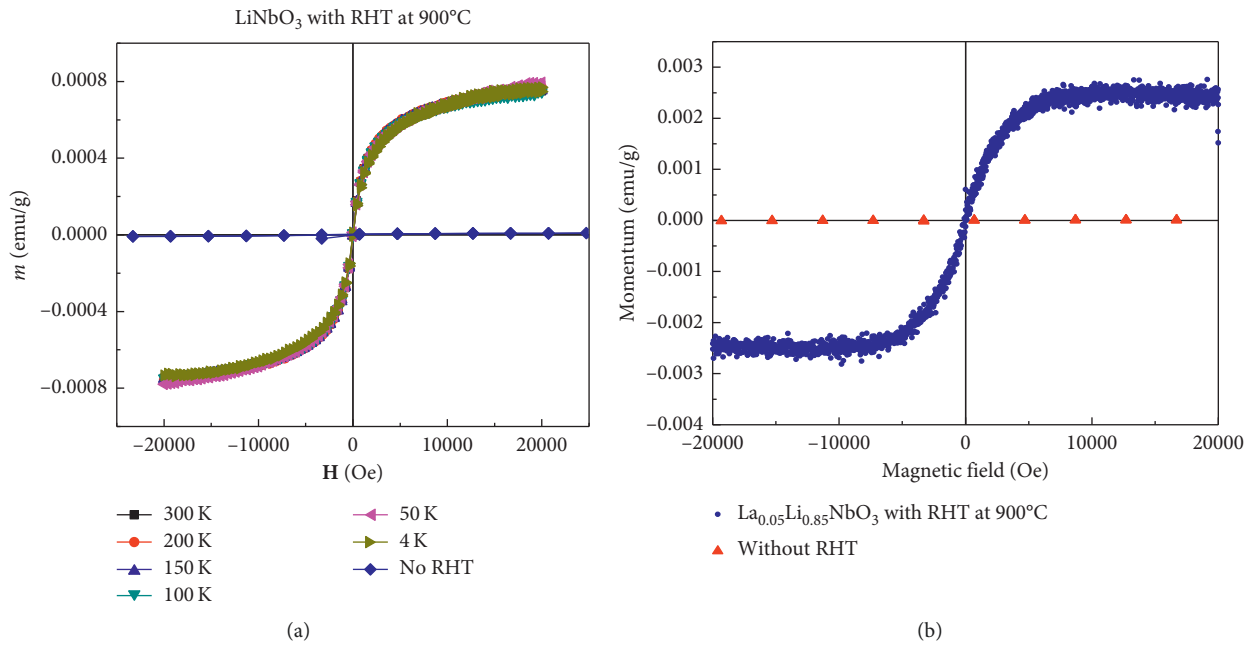FIGURE 5: Multiferroic properties; ferroelectrical hysteresis loop: (a) $LiNbO_3$ and (b) $La_{0.05}Li_{0.85}NbO_3$.

(a)

(b)

FIGURE 6: Multiferroic properties; magnetic hysteresis loop: (a) $LiNbO_3$ and (b) $La_{0.05}Li_{0.85}NbO_3$.

behavior is different from superparamagnetism, where anhysteretic magnetization curves taken at different temperatures must superpose only when plotted as a function of H/T. These ferromagnetic results are related to multiferroic properties due to the oxygen vacancies at the surface in $LiNbO_3$ and $La_{0.05}Li_{0.85}NbO_3$ nanocrystals, and they can be explained by the d-orbital contribution according to the XPS results. The creation of oxygen vacancies at the surface of nanocrystals in $LiNbO_3$ is strongly associated with the appearance of Nb^{+5}, Nb^{+4}, and Nb^{+3} valence states, and in $La_{0.05}Li_{0.85}NbO_3$, it is by Nb 3d-orbital and La 4d-orbital mainly. Both mechanisms act as charge reservoirs. The electronic spins can transfer ferromagnetism into the surface of $LiNbO_3$ and $La_{0.05}Li_{0.85}NbO_3$ nanoparticles, which is in close agreement with the result of Coey et al. [13]. No secondary magnetic impurity phase was found as previously

reported in [14, 31, 35]. In addition, the presence of lanthanum increases ferromagnetic signals when it is compared to pure lithium niobate ($LiNbO_3$).

3.3.3. Magnetocapacitance and Relaxor Ferroelectricity. The magnetocapacitive coupling and relaxor ferroelectricity properties due to oxygen vacancies were measured in $LiNbO_3$ and $La_{0.05}Li_{0.85}NbO_3$ nanocrystals, respectively. Figure 7(a) shows the magnetocapacitance effect of $LiNbO_3$ nanocrystals. It clearly shows an increase of the dielectric constant (κ) from 830 to 860 as a function of frequency and magnetic field. The magnetocapacitance effect is attributed to polarization of the d-orbital due to the ferroelectric-magnetic rich regions in response to the external magnetic field. The ferroelectric-magnetic dipoles are concentrated in
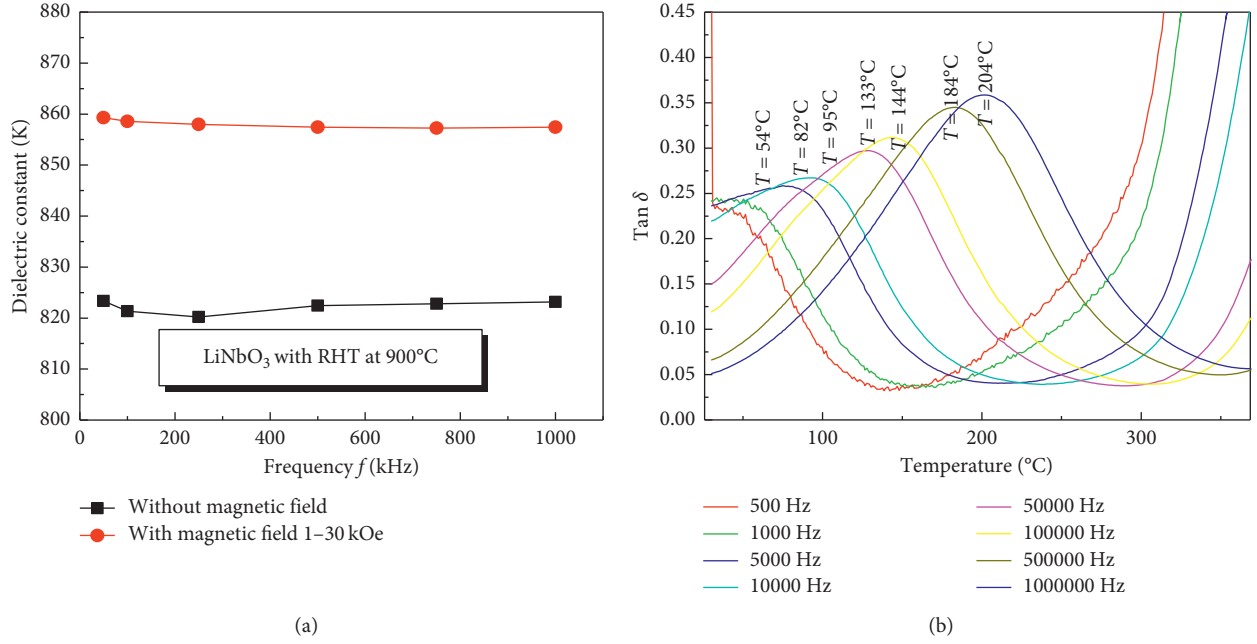
(a)

(b)

FIGURE 7: Multiferroic properties: (a) magnetocapacitance response of ferromagnetic $LiNbO_3$; (b) relaxor ferroelectricity properties in $La_{0.05}Li_{0.85}NbO_3$.

regions of grain boundaries and near the interfaces. In addition, the appearance of Nb^{+4} valences state is related to the ferro-paraelectric-magnetic phase responsible in the change of the dielectric constant of $LiNbO_3$ in presence of the magnetic field which is in complete agreement with the EELS result found.

On the contrary, Figure 7(b) shows the relaxor ferroelectricity properties of $La_{0.05}Li_{0.85}NbO_3$ nanocrystals from $25°C$ to $800°C$ in a frequency range from $100\,Hz$ to $1\,MHz$. The diffuse dielectric transitions is reported in the temperature range from $54°C$ to $204°C$, and the dielectric constant shifts from lower to higher values as frequency increases from $100\,Hz$ to $1\,MHz$. The dipole moment contributions are made by the orbitals Nb 3d, Li 1s, O 1s, La 4d, La 5s, and O 2s. These transition metal-oxygen bonds allow to relaxor-ferrolectric behavior in $La_{0.05}Li_{0.85}NbO_3$ nanoparticles.

This simultaneous presence of oxygen vacancies at the surface of $LiNbO_3$ and $La_{0.05}Li_{0.85}NbO_3$ nanocrystals lead to ferroelectric-ferromagnetic domains on crystallographical equivalent allowing the magnetocapacitance and relaxor ferroelectricity behavior, respectively, as previously reported [31, 34].

3.4. Second Harmonic Generation Properties of Multiferroic $LiNbO_3$ Nanocrystals. In multiferroic nanocrystals, single phase with magnetic and dielectric properties (or vice versa) require to have coupling between their electric susceptibility (χ_e) and magnetic susceptibility (χ_m). The electromagnetic wave as part of the optical field can lead to electronic origins of magnetic dipole stabilization and electric dipole transitions that can produce magneto-electric-optical phenomena use for the development of control devices [50].

3.4.1. Nonlinear Response of Multiferroic $LiNbO_3$ Nanocrystal Ceramic Materials. In multiferroic ABO_3 materials, the magnetic moment (M_s) and ferroelectric polarization (P_s) are achieved from 3d-orbital transition metals. The magnetic dipoles that occur in multiferroic materials can couple to an applied magnetic field and produce a collective magnetic moment different from zero ($M_s \neq 0$). On the contrary, the P_s is produce by cations located at the center of octahedron anions formed by oxygen atoms at the off-center positions, which produce a lattice distortion with a reordering of the electrons on the d-orbitals shell in direction of the applied electric field polarization [6, 9].

The magnetization can be divided into domains in which the individual's vectors are aligned according to local crystallographic easy axes as a volume density related to magnetic strength that is proportional to the magnetic field that causes them to be polarized in the field direction, according to

$$\mathbf{M} = \chi_m \mathbf{H}. \tag{3}$$

Figure 8(a) shows the magnetic susceptibility of multiferroic $LiNbO_3$ from $300\,K$ to $2\,K$ at a magnetic field of $1\,kOe$. The magnetic susceptibility, χ_m, at $300\,K$ is $6.56 \times 10^{-4}\,cm^3/mol$, in the range of $90\,K$ to $40\,K$ is $6.73 \times 10^{-4}\,cm^3/mol$, which is associated with anomalous structural feature previously observed at low temperatures by neutron diffraction experiments in $LiNbO_3$ [51], and at the temperature of $2\,K$ the χ_m is $8.33 \times 10^{-4}\,cm^3/mol$.

On the contrary, the optical response of a medium to an applied electromagnetic field can be expressed in terms of its polarization density $\mathbf{P}(t)$, which, in a linear dielectric medium, can be written linearly as
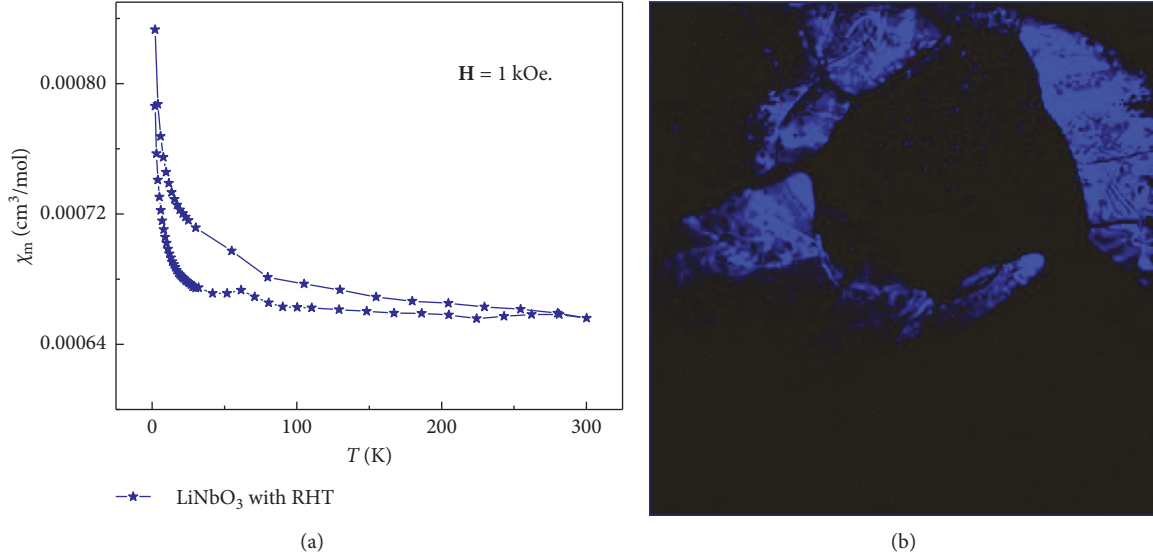
$$\mathbf{P}(t) = \chi_e^{(1)}\mathbf{E}(t), \tag{4}$$

(a)

(b)

FIGURE 8: (a) Magnetic susceptibility of multiferroic $LiNbO_3$ and (b) SHG revealed ferroelectric domains in multiferroic $LiNbO_3$ nanocrystals ceramic material.

where $\chi_e^{(1)}$ is the linear electric susceptibility and $\mathbf{E}(t)$ is the applied electric field. In a nonlinear material, the polarization density can be expressed as a Taylor expansion:

$$\mathbf{P}(t) = \chi_e^{(1)}\mathbf{E}(t) + \chi_e^{(2)}\mathbf{E}^2(t) + \cdots + \chi_e^{(n)}\mathbf{E}^n(t). \quad (5)$$

Replacing $\mathbf{E}(t)$ with $\mathbf{E}(e^{i\omega t} + \text{c.c})$, it is possible to find that a polarization field with double frequency 2ω is generated.

Figure 8(b) shows the second harmonic generation (SHG) of multiferroic $LiNbO_3$ nanocrystals ceramic material at horizontal linear polarization at $0°$. Here we use wavelength at 900 nm to generate SHG at 450 nm, related to blue color spectrum. The observed SHG intensity profile verifies the existence of fine structures (ferroelectric domains) in multiferroic $LiNbO_3$ nanocrystals ceramic material. Similar SHG results have been found in $La_{0.05}Li_{0.85}NbO_3$ nanocrystals ceramic material [52]; this crystal-symmetry-breaking process produces high-resolution images for domain patterns with angle polarization dependence.

Thus, the interaction of electromagnetic waves with single-phase multiferroic materials the electric susceptibility (χ_e) and magnetic susceptibility (χ_m) are densities of their dipoles related to the interaction with each other through their magnetic ($\mathbf{M}$) and electric ($\mathbf{P}$) fields, respectively. In materials with a high density of magnetic moments that couple spontaneously through short-range iterations related to the chemical bonding, a magnetization can exist without the presence of an applied $\mathbf{H}$ [49, 50].

3.4.2. Optical Properties of Multiferroic $LiNbO_3$ Nanocrystals. Finally, the second harmonic generation properties were also analyzed as a function of the wavelengths from 900 nm to 1200 nm at horizontal linear polarization in multiferroic $LiNbO_3$ nanocrystals. Figure 9(a) shows the case of laser

polarization of 900 nm of wavelength generating the SHG at 450 nm corresponding to blue color. Figure 9(b) shows the case of laser polarization of 1000 nm wavelengths generating the SHG at 500 nm corresponding to green color. Figure 9(c) repeats for laser wavelength of 1200 nm and a SHG at 600 nm corresponding to red color. Figure 9(d) shows the case of yellow color which is between the green and red color. This electro-optics effect found in $LiNbO_3$ nanocrystals is related to oxygen vacancies that can be explained by the electronic structure contribution of Nb 3d-orbital related to Nb^{5+}, Nb^{4+}, and Nb^{3+} ions and O 1s-orbital. In addition, oxygen vacancies contain a two-electron trap, which produce intrinsic voids related to reordering of lithium, niobium, and oxygen ions in the sublattice leading to neutral charge defects. It is worth mentioning that $LiNbO_3$ nanocrystals without RHT only showed blue SHG signal. These results were in complete agreement with previous studies in $La_{0.05}Li_{0.85}NbO_3$ nanocrystals [31, 45].

4. Conclusions

In this work, we successfully synthesized $La_{0.05}Li_{0.85}NbO_3$ and $LiNbO_3$ nanocrystals with multiferroic-optic properties by using the mechanochemical method. The structural aspects and multiferroic-optics properties were analyzed by using Cs-corrected scanning electron microscope, electron energy loss spectroscopy, Raman spectroscopy, X-ray photoelectron spectroscopy, and second harmonic generation microscope, respectively. The Raman spectroscopy results showed a well-formed ABO_3 perovskites crystal structure of $LiNbO_3$ and $La_{0.05}Li_{0.85}NbO_3$ nanocrystals; it was found that the vibrational modes at 276, 322 (323), and 625 (624) cm^{-1} corresponding to the vibration modes A_1 [TO_2], A_1 [TO_3], and A_1 [TO_4] associated to the loss of symmetry of the oxygen site that is produced during the RHT. The XPS spectroscopy results showed the electronic
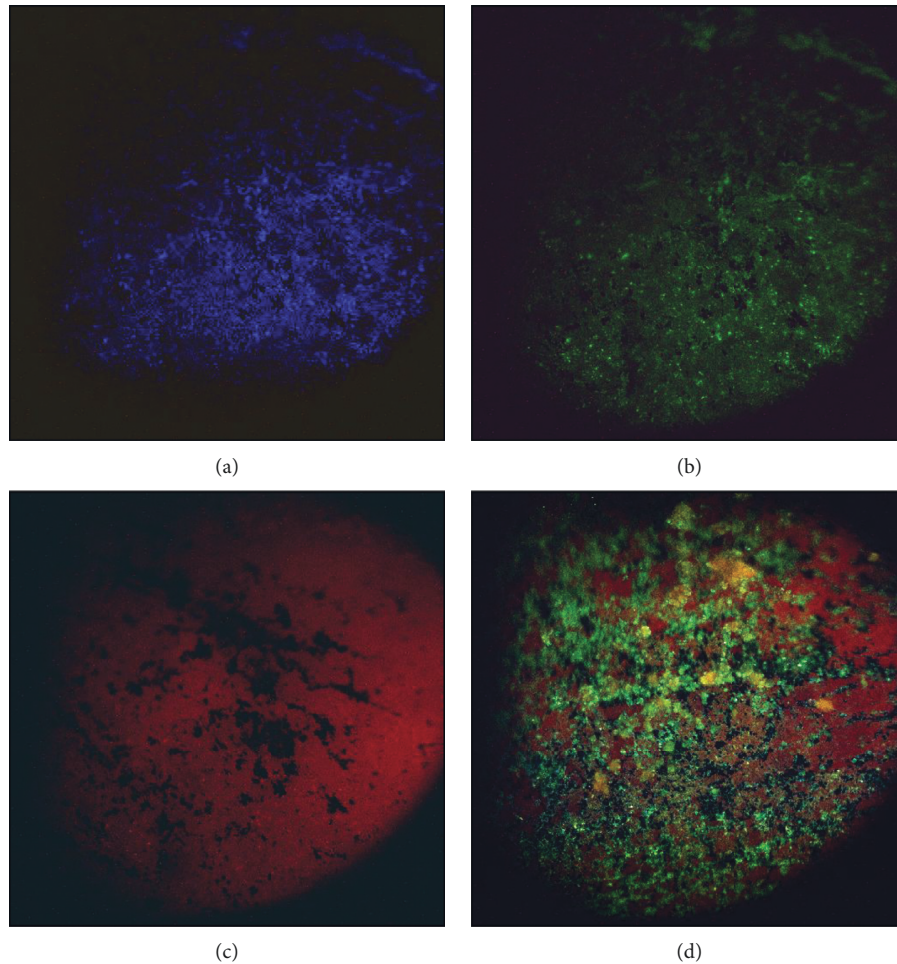
FIGURE 9: Multiferroic LiNbO$_3$ SHG properties: (a) blue color, (b) green color, (c) red color, and (d) overlap between green and red, showing yellow color.

orbital structure of lithium (Li^{+1}), lanthanum (La^{+3}), niobium (Nb^{+5}), and oxygen (O^{-2}) in multiferroic LiNbO$_3$ and La$_{0.05}$Li$_{0.85}$NbO$_3$ nanocrystals, respectively. With Cs-corrected STEM, it was possible to determine structural changes related to oxygen vacancies at the surface of LiNbO$_3$ nanocrystals. With EELS, it was possible to determine the core-shell electronic density of core (1.79×10^{29} electron/m^3) and shell (1.33×10^{29} electron/m^3), respectively. Also, it was found that Nb^{+4} is related to paraelectric phase transition, which confirms the presence of oxygen vacancies at the surface of multiferroic LiNbO$_3$ nanocrystals. With SHG microscope, ferroelectric domains were found at 450 nm in multiferroic LiNbO$_3$ nanocrystals ceramic material. Also, it was found the SHG signals in LiNbO$_3$ nanocrystals at 450 nm, 500 nm, and 600 nm corresponding to blue, green, and red color, respectively. Also, the yellow color was found when overlapping the SGH signals at 500 nm and 600 nm. In summary, the observed values of ferroelectric, high-ferromagnetism temperature, magnetocapacitance, relaxor ferroelectricity, ferroelectric-optic, and multiferroic optics found in stoichiometric lanthanum lithium niobate and lithium niobate may be useful for development of new multiferroic: ferroelectric-magneto-optical control devices.

Conflicts of Interest

The authors declare that they have no conflicts of interest.

Acknowledgments

Supplementary Materials

Supplementary 1. Video 1: SHG results studied as a function of laser linearly and circularly polarized under different excitation-dependent polarization in multiferroic stoichiometric LiNbO$_3$ nanocrystals ceramic material.
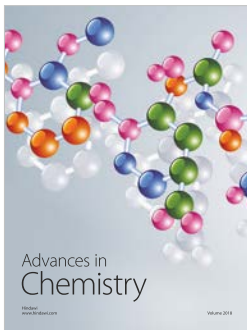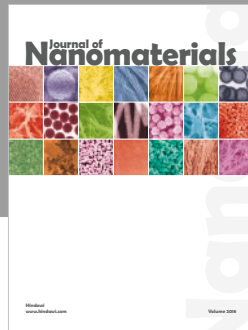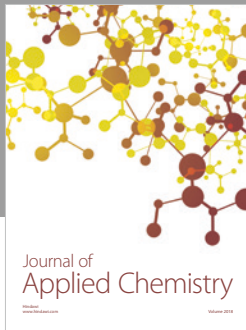
Supplementary 2. Video 2: ferroelectric domains stripe pattern by SHG in ferromagnetic stoichiometric $LiNbO_3$ nanocrystals ceramic material.

Supplementary 3. Video 3: SHG results in multiferroic stoichiometric $LiNbO_3$ nanocrystals.

References

[1] M. Fiebig, T. Lottermoser, D. Meier, and M. Trassin, "The evolution of mutliferroics," *Nature Reviews Materials*, vol. 1, no. 8, pp. 1–14, 2016.

[2] J. Shen, J. Cong, D. Shang et al., "A Multilevel nonvolatile magnetoelectric memory," *Scientific Reports*, vol. 6, no. 1, article 34473, 2016.

[3] H. Schmid, "Multi-ferroic magnetoelectrics," *Ferroelectrics*, vol. 162, no. 1, p. 317, 1994.

[4] M. Fiebig, Th. Lottermoser, D. Fröhlic, A. V. Goldzev, and R. V. Pisarev, "Observation of coupled magnetic and electric domains," *Nature*, vol. 419, no. 6909, pp. 818–820, 2002.

[5] J. M. D. Coey, P. Stamenov, R. D. Gunning, M. Venkatesanand, and K. Paul, "Ferromagnetism in defect-ridden oxides and related materials," *New Journal of Physics*, vol. 12, no. 5, p. 14, 2010.

[6] H. Schmid, "Some symmetry aspects of ferroics and single phase multiferroics," *Journal of Physics: Condensed Matter*, vol. 20, no. 43, article 434201, 2008.

[7] A. Planes, L. Mañosa, and A. Saxena, *Magnetism and Structure in Functional Materials*, Springer-Verlag, Berlin, Heidelberg, Germany, 2005.

[8] A. Kargol, L. Malkinski, and G. Caruntu, "Biomedical applications of multiferroic nanoparticles," *Advanced Magnetic Materials*, InTech, Croatia, 1st edition, 2012, ISBN: 978-953-51-0637-1.

[9] Y. Xu, *Ferroelectric Materials and Their Applications*, North-Holland, Amsterdam, Netherlands, 1st edition, 1991.

[10] M. E. Lines and A. M. Glass, *Principles and Applications of Ferroelectrics and Related Materials*, Clarendon Press, Oxford, UK, 1977.

[11] T. Volk and M. Wöhlecke, *Lithium Niobate*, Springer-Verlag, Berlin, Germany, 1st edition, 2008.

[12] M. Hayashi, L. Thomas, R. Moriya, C. Rettner, and S. S. Parkin, "Current-controlled magnetic domain-wall nanowire shift register," *Science*, vol. 320, no. 5873, pp. 209–211, 2008.

[13] J. M. D. Coey, J. T. Mlack, M. Venkatesan, and P. Stamenov, "Magnetization process in dilute magnetic oxides," *IEEE Transactions on Magnetics*, vol. 46, no. 6, pp. 2501–2503, 2010.

[14] W. Eerenstein, N. D. Mathur, and J. F. Scott, "Multiferroic and magnetoelectric materials," *Nature*, vol. 442, no. 7104, pp. 759–765, 2006.

[15] N. A. Sapalding and M. Fiebig, "Materials science: the renaissance of magnetoelectric multiferroics," *Science*, vol. 309, no. 5733, pp. 391-392, 2005.

[16] A. Sundaresan and C. N. R. Rao, "Ferromagnetism as a universal feature of inorganic nanoparticle," *Nano Today*, vol. 4, no. 1, p. 96, 2009.

[17] B. Knabe, D. Schütze, T. Jungk et al., "Synthesis and characterization of Fe-doped $LiNbO_3$ nanocrystals from a triple-alkoxide method," *Physica Status Solidi*, vol. 208, no. 4, pp. 857–862, 2011.

[18] A. Rüdiger and R. Waser, "Size effects in nanoscale ferro-electrics," *Journal of Alloys and Compounds*, vol. 449, no. 1-2, pp. 2–6, 2008.

[19] W. Zhou, M. P. Oxley, A. R. Lupini, O. L. Krivanek, S. J. Pennycook, and J.C. Idrobo, "Single atom microscopy," *Microscopy and Microanalysis*, vol. 18, no. 6, pp. 1342–1354, 2012.

[20] R. F. Egerton, "Electron energy-loss spectroscopy in TEM," *Reports on Progress in Physics*, vol. 72, no. 1, article 016502, 2009.

[21] J. López and M. Castro, *Surface Spectroscopy for Engineers and Scientists*, CreateSpace Publishing, Scotts Valley, CA, USA, 2013, ISBN 978-1483999968.

[22] P. S. Dobal and R. S. Katiyar, "Studies on ferroelectric perovskites and bi-layered compounds using micro-Raman spectroscopy," *Journal of Raman Spectroscopy*, vol. 33, no. 6, pp. 405–423, 2002.

[23] R. W. Boyd, *Nonlinear Optics*, Academic Press, Cambridge, MA, USA, 3rd edition, 2008.

[24] Y. Zhu, C. Song, A.M. Minor, and H. Wang, "Cs-corrected scanning transmission electron microscopy investigation of dislocation core configurations at a $SrTiO_3$/MgO heterogeneous interface," *Microscopy and Microanalysis*, vol. 19, no. 3, pp. 706–715, 2013.

[25] A. A. Bokov and Z. G. Ye, "Recent progress in relaxor ferroelectric with perovskite structure," *Journal of Materials Science*, vol. 41, no. 1, pp. 31–52, 2006.

[26] C. Song, F. Zeng, Y. X. Shen et al., "Local Co structure and ferromagnetism in ion-implanted Co-doped $LiNbO_3$," *Physical Review B*, vol. 73, no. 17, article 172412, 2006.

[27] T. Kimura, S. Kawamoto, I. Yamada, M. Azuma, M. Takano, and Y. Tukura, "Magnetocapacitance effect in multiferroic $BiMnO_3$," *Physical Review B*, vol. 67, no. 18, article 180401, 2003.

[28] R. V. K. Mangalam, N. Ray, U. V. Waghmare, A. Sundaresan, and C. N. R. Rao, "Multiferroic properties of nanocrystalline $BaTiO_3$," *Solid State Communications*, vol. 149, no. 1-2, pp. 1–5, 2009.

[29] R. K. Nath, M. F. M. Zain, and A. A. H. Kadhum, "Artificial photosynthesis using $LiNbO_3$ as photocatalyst for suistanable and environmental friendly construction and reduction of global warming: a review," *Catalysis Reviews*, vol. 56, no. 2, pp. 175–186, 2014.

[30] K. Saito, K. Koga, and A. Kudo, "Lithium niobate nanowires for photocatalytic water splitting," *Dalton Transactions*, vol. 40, p. 3909, 2011.

[31] C. A. Díaz-Moreno, J. Portelles, C. Li et al., "Relaxor ferroelectricity, ferromagnetic and optical second harmonic properties in lanthanum lithium niobate ($La_{0.05}Li_{0.85}NbO_3$) nanoparticles," *Journal of Magnetism and Magnetic Materials*, vol. 433, pp. 262–270, 2017.

[32] C. A. Díaz-Moreno, A. Hurtado-Macias, R. Farias, J. Hernandez-Paz, and J. Elizalde-Galindo, "Multiferroic response of nanocrystalline lithium niobate," *Journal of Applied Physics*, vol. 111, no. 7, article 07D907, 2012.

[33] F. Espinosa-Magaña, C. A. Díaz-Moreno, V. Gallegos, A. Santos, J. Farias, and F. Delgado, "Study of electronic structure of $LiNbO_3$ nanoparticles by EELS," *Microscopy and Microanalysis*, vol. 19, no. 2, pp. 1966-1967, 2013.

[34] C. A. Díaz-Moreno, J. González-Hernández, R. Escudero et al., "Magnetocapacitance effect in ferromagentic $LiNbO_3$ nanoparticles," *Journal of Magnetism and Magnetic Materials*, vol. 407, pp. 291–298, 2016.

[35] C. A. Díaz Moreno, J. A. Matutes-Aquino, F. Espinosa-Magaña et al., "Magnetic behaviour in $LiNbO_3$ nanocrystallites caused by oxygen vacancies," *Journal of Magnetism and Magnetic Materials*, vol. 356, pp. 82–86, 2014.

[36] A. Sundaresan, R. Bhargavi, N. Rangarajan, U. Siddesh, and C. Rao, "Ferromagnetism as a universal feature of nanoparticles of the otherwise nonmagnetic oxide," *Physical Review B*, vol. 74, no. 16, article 161306, 2006.

[37] J. Hemberger, P. LunKenheimer, R. Fichtl, H. A. Krug von Niddia, V. Tsurkan, and A. Loidl, "Relaxor ferroelectricity and colossal magnetocapacitive coupling in ferromagnetic $CdCr_2S_4$," *Nature*, vol. 434, no. 7031, pp. 364–367, 2005.

[38] D. H. Wang, W. C. Goh, M. Ning, and C. K. Ong, "Effect of Ba doping on magnetic, ferroelectric and magnetoelectric properties in multiferroic $BiFeO_3$ at room temperature," *Applied Physics Letters*, vol. 88, no. 21, article 212907, 2006.

[39] S. Sanna and W. G. Schmidt, "Lithium niobate X-cut, Y-cut and Z-cut surfaces from ab initio theory," *Physical Review B*, vol. 81, no. 21, pp. 1–11, 2010.

[40] M. A. Mukhtarov, K. N. Pilipchak, and E. V. Zolotukhin, "Electron energy losses in lithium nobate," *Journal of Physics and Chemistry of Solids*, vol. 59, no. 8, pp. 1219–1227, 1998.

[41] V. Gallegos Orozco, R. Martinez Sanchez, and F. Espinosa Magana, "In situ characterization of the ferroelectric transition in $BaTiO_3$ by EELS and comparison with ab initio methods," *Physical Review B*, vol. 77, no. 4, article 045128, 2008.

[42] F. C. Vasquez, V. Gallegos Orozco, C. Ornelas Gutierrez, W. Antunez Flores, A. Beltran, and F. Paraguay Delgado, "Zinc doped SnO_2 electronic structure study by EELS," *Microscopy and Microanalysis*, vol. 19, no. 2, p. 1586, 2013.

[43] S. G. Bahoosh and J. M. Wesselinowa, "The origin of magnetism in perovskites ferroelectric ABO_3 nanoparticles (A = K,Li; B = Ta, Nb or A = Ba,Sr; B = Ti)," *Journal of Applied Physics*, vol. 122, no. 5, article 053907, 2012.

[44] Y. Repelin, E. Husson, F. Bennani, and C. Proust, "Raman spectroscopy of lithum niobate and lithium tantalate force field calculations," *Journal of Physics and Chemistry of Solids*, vol. 60, no. 6, pp. 819–825, 1999.

[45] C. A. Díaz-Moreno, C. Li, J. Portelles et al., "Optical properties of ferroelectric lanthanum lithium niobate," *Ceramic International*, vol. 44, no. 1, pp. 4727–4733, 2018.

[46] R. Courths, P. Steiner, H. Höchst, and S. Hüfner, "Photoelectron-spectroscopy investigation and electronic properties of $LiNbO_3$ crystal surfaces," *Applied Physics*, vol. 21, no. 4, pp. 345–352, 1980.

[47] P. Steiner and H. Höechst, "X-ray excited photoelectron spectra of $LiNbO_3$: a quantitative analysis," *Zeitschrift für Physik B Condensed Matter*, vol. 35, no. 1, pp. 51–59, 1979.

[48] K. Tabata, M. Kamada, T. Choso, and H. Munakata, "Photoelectron spectroscopy investigation of NO adsorption defects of LiNbO3 surfaces," *Applied Surface Science*, vol. 125, no. 1, pp. 93–98, 1998.

[49] K. Ackland, L. M. A. Monzon, M. Venkatesan, and J. M. D. Coey, "Magnetism of nanostructure CeO_2," *IEEE Transactions on Magnetics*, vol. 47, no. 10, pp. 3509–3512, 2011.

[50] G. F. Dionne, *Magnetic Oxides*, Springer Science, Secaucus, NJ, USA, 1st edition, 2009.

[51] R. Fernandez Ruiz, D. Martin, and V. Bermudez, "Anomalous structural feature of $LiNbO_3$ observed using neutron diffraction," *Physical Review B*, vol. 72, no. 18, article 184108, 2005.

[52] S. W. Liu, J. Chakhalian, and M. Xiao, "Second Harmonic generation and ferroelectric phase transitions in thick and ultrathin $Pb_{0.35}Sr_{0.65}TiO_3$ films on (001) MgO substrate," *Applied Physics Letters*, vol. 90, no. 4, article 042901, 2007.